



Inclusion of material non-linearity and inelasticity into a continuum-level material model for soda-lime glass

M. Grujicic ^{a,*}, W.C. Bell ^a, B. Pandurangan ^a, B.A. Cheeseman ^b, P. Patel ^b, G.A. Gazonas ^b

^aDepartment of Mechanical Engineering, Clemson University, Clemson, SC 29634, United States

^bArmy Research Laboratory – Survivability Materials Branch, Aberdeen, Proving Ground, MD 21005-5069, United States

ARTICLE INFO

Article history:

Received 11 July 2011

Accepted 19 August 2011

Available online 7 September 2011

Keywords:

Glasses

Fracture

Modeling

ABSTRACT

Numerous experimental investigations clearly established that when soda-lime glass is subjected to sufficiently high axial-stress/pressure, it displays a nonlinear mechanical response and deformation irreversibility (inelasticity). This portion of the material behavior is often neglected in material models for glass which tend to focus on the damage and fracture phenomena of the material. However, material nonlinearity/inelasticity can, in principle, have a profound effect on wave/shock propagation phenomena and processes (e.g. spall fracture).

Within the present work, the effect of material nonlinearity and inelastic behavior on the dynamic response (including spallation) of soda-lime glass is studied under symmetric flyer-plate loading conditions using computational methods and tools. Material nonlinearity and deformation irreversibility are modeled in two different ways: (a) as a non-linear elastic material response with no deformation irreversibility; and (b) as a linear-elastic, volumetrically-plastic deformation response. Incorporation of nonlinearity and inelasticity phenomena into a continuum-level material model for soda-lime glass recently developed by the authors revealed that while these phenomena do not measurably affect spall resistance (as measured by a minimum flyer-plate velocity resulting in spallation), they provide beneficial linear-momentum/kinetic energy reduction effects.

© 2011 Elsevier Ltd. All rights reserved.

1. Introduction

Contemporary transparent armor is typically composed of a system of materials designed to meet a set of optical transparency constraints while providing a compulsory level of protection against blast and ballistic/fragment impacts. This class of protective materials is employed in varied applications from personal protective visors for combat/non-combat usage (e.g. riot control or explosive ordnance disposal) to vehicle/structure transparent-armor systems (vehicle windows designed to protect occupants and on-board instruments/sensors from projectiles and/or fragment impacts during combat/terrorist attacks or other hostile conflicts). Recent engagements of the US military forces in the Operation Iraqi Freedom and Operation Enduring Freedom (Afghanistan) have highlighted the critical importance of transparent armor. Persistent escalations in the number and variety of threats along with constricting military budget have greatly increased the need for rapidly-deployable, threat-specific, weight-/cost-performance-optimized transparent armor and armor

systems. These threats to US military's safety have motivated great amount of research effort within US and abroad focused on accelerating the development of novel/enhanced transparent armor systems.

Historically, transparent armors have been based on monolithic glass or, more recently, transparent-elastomer inter-layered glass laminates. Numerous advancements within the class of transparent-armor materials and novel technologies have been reported within open literature, of which the following have received the most attention: crystalline ceramics (e.g. aluminum-oxinitride spinel, AlON [1]), novel transparent polymer materials (e.g. transparent nylon [2]), new interlayer/adhesive materials (e.g. polyurethane bonding layers [1]), and new laminate designs e.g. [3]. In the face of increasing demands for improvements in ballistic-protection performance of transparent armor, and the concomitant requirements for improved performance to weight ratios that call for the use of new transparent materials (e.g. transparent crystalline ceramics), advanced transparent polymeric materials and advanced technologies (e.g. multi-material functionally-graded laminated transparent armor), glass (as well as glass ceramics) continues to retain its role as a popular material choice in ground-vehicle transparent armor applications. The main reason for the continued use of glass in transparent-armor applications have been discussed in our recent work [4,5].

* Corresponding author. Address: 241 Engineering Innovation Building, Clemson University, Clemson, SC 29634-0921, United States. Tel.: +1 864 656 5639; fax: +1 864 656 4435.

E-mail address: gmica@clemson.edu (M. Grujicic).

Report Documentation Page			Form Approved OMB No. 0704-0188	
<p>Public reporting burden for the collection of information is estimated to average 1 hour per response, including the time for reviewing instructions, searching existing data sources, gathering and maintaining the data needed, and completing and reviewing the collection of information. Send comments regarding this burden estimate or any other aspect of this collection of information, including suggestions for reducing this burden, to Washington Headquarters Services, Directorate for Information Operations and Reports, 1215 Jefferson Davis Highway, Suite 1204, Arlington VA 22202-4302. Respondents should be aware that notwithstanding any other provision of law, no person shall be subject to a penalty for failing to comply with a collection of information if it does not display a currently valid OMB control number.</p>				
1. REPORT DATE 2012	2. REPORT TYPE	3. DATES COVERED 00-00-2012 to 00-00-2012		
4. TITLE AND SUBTITLE Inclusion of material non-linearity and inelasticity into a continuum-level material model for soda?lime glass		5a. CONTRACT NUMBER		
		5b. GRANT NUMBER		
		5c. PROGRAM ELEMENT NUMBER		
6. AUTHOR(S)		5d. PROJECT NUMBER		
		5e. TASK NUMBER		
		5f. WORK UNIT NUMBER		
7. PERFORMING ORGANIZATION NAME(S) AND ADDRESS(ES) Clemson University,Department of Mechanical Engineering,241 Engineering Innovation Building,Clemson,SC,29634		8. PERFORMING ORGANIZATION REPORT NUMBER		
9. SPONSORING/MONITORING AGENCY NAME(S) AND ADDRESS(ES)		10. SPONSOR/MONITOR'S ACRONYM(S)		
		11. SPONSOR/MONITOR'S REPORT NUMBER(S)		
12. DISTRIBUTION/AVAILABILITY STATEMENT Approved for public release; distribution unlimited				
13. SUPPLEMENTARY NOTES				
14. ABSTRACT <p>Numerous experimental investigations clearly established that when soda?lime glass is subjected to sufficiently high axial-stress/pressure, it displays a nonlinear mechanical response and deformation irreversibility (inelasticity). This portion of the material behavior is often neglected in material models for glass which tend to focus on the damage and fracture phenomena of the material. However, material nonlinearity/ inelasticity can, in principle, have a profound effect on wave/shock propagation phenomena and processes (e.g. spall fracture). Within the present work, the effect of material nonlinearity and inelastic behavior on the dynamic response (including spallation) of soda?lime glass is studied under symmetric flyer-plate loading conditions using computational methods and tools. Material nonlinearity and deformation irreversibility are modeled in two different ways: (a) as a non-linear elastic material response with no deformation irreversibility and (b) as a linear-elastic, volumetrically-plastic deformation response. Incorporation of nonlinearity and inelasticity phenomena into a continuum-level material model for soda?lime glass recently developed by the authors revealed that while these phenomena do not measurably affect spall resistance (as measured by a minimum flyer-plate velocity resulting in spallation), they provide beneficial linarmomentum/ kinetic energy reduction effects.</p>				
15. SUBJECT TERMS				
16. SECURITY CLASSIFICATION OF:			17. LIMITATION OF ABSTRACT Same as Report (SAR)	
a. REPORT unclassified	b. ABSTRACT unclassified	c. THIS PAGE unclassified	18. NUMBER OF PAGES 12	19a. NAME OF RESPONSIBLE PERSON

It is well understood that glass exhibits markedly different behavior under quasi-static (i.e. low deformation-rate) and dynamic (i.e. high deformation-rate) loading conditions e.g. [6–12]. Main differences in glass behavior within the two loading rate ranges have been discussed in our recent work [4,5]. Furthermore, the physics of glass behavior in these two regimes has been utilized in Refs. [4,5] to construct a continuum-type material model for glass.

A comprehensive literature review carried out as part of the present work revealed that the mechanical behavior of glass is modeled predominantly using three distinct approaches: (a) molecular-modeling methods [13–19]; (b) continuum-level finite element material approximations [20–24,26,27], and (c) finite-element modeling of explicit cracks [25]. A brief overview and the main findings for each of these three approaches can be found in our recent work [4,5]. The present work deals with the continuum-level glass models which are generally used in large scale simulations of the ballistic performance of transparent armor systems.

As mentioned earlier, a continuum-level material model for glass has been proposed in our recent work [4,5]. The main objective of the present work is to extend this model in order to include the phenomena of material non-linearity and deformation-irreversibility. To assess the contribution of these phenomena to the dynamic behavior of glass, computational flyer-plate experiments are carried out and the spallation fracture process monitored.

The organization of the paper is as follows: An overview of the soda-lime glass material model of Grujicic et al. [4,5] is provided in Section 2. The incorporation of the material-nonlinearity and deformation inelasticity effects into the material model of Grujicic et al. [4,5] is presented in Section 3. Details of a transient nonlinear dynamics computational analysis of a flyer-plate impact experiment used to validate the enhancements to the material model for soda-lime ballistic glass are discussed in Section 4. The main results obtained in the present work are presented and discussed in Section 5. The key conclusions resulted from the present work are summarized in Section 6.

2. Soda-lime glass model of Grujicic et al. [4,5]

This section focuses on: (a) the main features of the soda-lime glass material model developed by Grujicic et al. [4,5]; (b) the procedure used to derive the fundamental equations which govern the material mechanical response; and (c) the approach used to gather the necessary experimental data and carry-out material-model parameterization.

2.1. Damage/failure physics of soda-lime glass

The soda-lime glass model of Grujicic et al. [4,5], tries, in a computationally-efficient manner, to incorporate the experimentally well-documented differences in the behavior of glass when subjected to low deformation-rate (quasi-static) and high deformation-rate (dynamic) loading conditions. Specifically, it is well-established that, under quasi-static loading conditions, failure of glass is associated with the formation/propagation of few cracks and the complete fracture yields few fragments. On the other hand, under dynamic loading conditions, glass failure/fracture is preceded by extensive damage (associated with the formation of numerous micron and submicron-size cracks). The complete fracture, in this case, is associated with comminution (i.e. formation of a large number of sub-millimeter size fragments). Nevertheless, under both low- and high-loading rates, damage-initiation as well as failure/fracture are believed to be controlled by pre-existing

material defects/flaws. These flaws can become propagating cracks when subjected to sufficiently high stresses. More details regarding the basic physics of glass deformation and fracture behavior in the quasi-static and dynamic loading conditions can be found in Refs. [4,5].

2.2. Key components of the material model

A detailed analysis of the key components of the material model of Grujicic et al. [4,5] including failure (bulk and surface) probability distribution function, crack nucleation criteria, crack growth kinetics, damage initiation and evolution equations, etc. can be found in Refs. [4,5].

2.3. Mathematical formulation of the model

2.3.1. Coarse-fragmentation failure/fracture mode

As discussed earlier, under quasi-static loading conditions, soda-lime glass typically fails via the coarse-fragmentation mode associated with the nucleation and propagation of a few (macro) cracks. This behavior of glass was rationalized as follows: Under low-loading rates, the rate of increase of stress is also low. Hence, when the first crack nucleates it begins to propagate (at a terminal velocity, typically equal to 0.2–0.4 of the corresponding sound speed) and grow its shielding zone (within which the stresses are reduced and the potential crack nucleating flaws made inactive). Meanwhile, stresses in the unshielded regions of the material do not frequently reach high-enough values to cause nucleation of new cracks. Consequently, the material fails via the coarse-fragmentation mode.

Clearly, in this loading regime fracture strength corresponds to the stress-level at which the first crack forms. The stress at which the first crack forms, on the other hand, is a function of the potency/size of the crack-nucleating flaw. Consequently, the material fracture strength becomes a stochastic quantity which is defined by an appropriate failure-distribution function, rather than by a mean value. Within the soda-lime glass material model of Grujicic et al. [4,5], the coarse-fragmentation mode failure-probability function is represented using a two-parameter Weibull-distribution function. This function was derived by treating the crack nucleation phenomenon as a Poisson point-process and is given by the following expression:

$$P_F = 1 - \exp[-\lambda_t Z] \quad (1)$$

where the failure probability P_F represents the probability of finding at least one crack-nucleating defect in the material region/domain of size Z and λ_t is the stress-dependent defect-density and is expressed as:

$$\lambda_t = \lambda_0 \left(\frac{\sigma}{S_0} \right)^m \quad (2)$$

where λ_0 is the reference defect density, S_0 is a stress normalizing parameter and m is the Weibull modulus.

The failure probability distribution function (which is equal to the fracture-strength cumulative distribution function) is obtained by substituting Eq. (2) into Eq. (1). The fracture strength probability density function is then obtained by differentiating the resulting equation with respect to sigma. It should be noted that despite an explicit appearance of three parameters (λ_0 , S_0 , m), the Weibull distribution function contains only two independent parameters (m and $S_0/\lambda_0^{1/m}$). Next, using the standard mathematical relations for the single-variant mean value and standard deviation, the following expressions for the fracture-strength mean value and standard deviation are derived [18]:

$$\sigma_{f,static} = \frac{S_0}{(Z_{eff} \lambda_0)^{1/m}} \Gamma \left(1 + \frac{1}{m} \right) \quad (3)$$

and

$$\sigma_{sd} = \sqrt{\frac{S_0^2}{(Z_{eff}\lambda_0)^{2/m}} \Gamma\left(1 + \frac{2}{m}\right) - \sigma_{f,static}^2} \quad (4)$$

where Γ denotes the gamma function which is defined as:

$$\Gamma(x) = (x-1)! \quad (5)$$

As discussed earlier, to model the growth of macro-cracks beyond the length of a single element, the stress-based fracture initiation criterion defined above is combined with a linear-elastic fracture-mechanics based crack growth criterion. The procedure used to implement the later criterion involves the following steps: (a) first, adjacent failed elements aligned in a particular direction are used to define the associated crack length ($2a$) in that direction. Seven possible directions are considered, three of which are aligned with the edges and the remaining four with the diagonals of the cube-shaped finite element; (b) for an element located at a crack tip, the stress intensity factor K_I is calculated by multiplying its maximum principal stress with a factor $\sqrt{\pi a}$; (c) when the condition $K_I > K_{IC}$, where K_{IC} is the mode I critical stress intensity factor is satisfied, the fracture of the element is initiated. As in the case of the stress-based fracture criterion, the complete fracture of the element and its removal is governed by the crack terminal velocity.

2.3.2. Fine-fragmentation/communition failure/fracture mode

As discussed earlier, under dynamic loading conditions, soda-lime glass typically fails via the fine-fragmentation mode associated with the nucleation and propagation of numerous (micro) cracks. This behavior of glass was rationalized as follows: Under high-loading rates, the rate of increase of stress is also high. Hence, before the first nucleated cracks can advance (and enlarge their shielding zones) considerably, stresses in unshielded material regions becomes high enough to cause nucleation of numerous cracks. Consequently, the material fails via the fine-fragmentation mode. It should be also noted that the neighboring cracks with compatible opening modes and orientations may, via their shielding zone, mutually terminate each other's growth, giving rise to relatively short cracks.

Based on the description provided above, it was concluded that failure and ultimate fracture of glass in this loading regime should be modeled as a progressive-damage process rather than a brittle-fracture process (adopted in the coarse fragmentation mode). This was done in the soda-lime glass material model of Grujicic et al. [4,5]. The specifics of this material model in the high-loading rate regime are discussed in the remainder of this section and involve the following points:

- (a) When a crack-nucleating flaw is activated and the crack begins to grow, a crack-surrounding shielding zone is formed and increases in size. Within the model, stresses within the shielding zone are assumed to relax to zero and, hence, activation of any flaw residing within this zone will be suppressed.
- (b) The size of the shielding-zone (assumed to be of a spherical shape for bulk flaws and of a circular shape for surface cracks) is postulated to increase during crack propagation, in a self-similar manner. Therefore, the shielding-zone size at a time t associated with a crack which was nucleated at the time τ is defined as:

$$Z_{sh}(t, \tau) = S[kC(t - \tau)]^n \quad (6)$$

where $C = [E/\rho]^{0.5}$ is the speed of sound, E the Young's modulus, ρ the mass density, $k = 0.2–0.4$, the crack terminal speed to sound speed ratio, n is the domain-dimensionality factor for the

fracture-controlling flaws (=2, for surface failure and =3, for bulk failure) and S is a shielding zone shape factor (= $4\pi/3$, for a spherical bulk zone and π for a circular shielding zone);

- (c) Due to the stress-relaxation within the shielding zones, distinction is made between the potentially crack-nucleating (unshielded) and the deactivated (shielded) flaws so that the total flaw density can be decomposed as:

$$\lambda_t = \lambda_{non-sh} + \lambda_{sh} \quad (7)$$

where both λ_{non-sh} and λ_{sh} are defined by dividing the corresponding number of flaws by the total domain size;

- (d) The rate of loading affects the relative magnitude of the unshielded and shielded flaw densities as follows: (i) under low-loading rates, a large fraction of the flaws will become inactive (due to the presence of large shielding zone(s)) and under quasi-static loading conditions all flaws (except for the one(s) associated with the nucleation of first crack(s)) will become shielded. This, in turn, would yield a relatively large value of λ_{sh} ; and (ii) under high-loading rate conditions, the shielding zone(s) are relatively small leading to a relatively large value of λ_{non-sh} .

- (e) In contrast to the coarse-fragmentation mode for which the mean fracture strength, defined by Eq. (3), is assumed to be constant (but to take different values in the surface and bulk material regions), the dynamic fracture strength is found to be a loading-rate dependent quantity. The functional form for the dynamic fracture strength is given below.

- (f) To derive an expression for the dynamic fracture strength, a uniform constant-loading rate ($\dot{\sigma} = \text{constant}$) case was analyzed first. Also distinction is made between the externally-applied macroscopic stress, Σ , and its internal counterpart $\sigma = \dot{\sigma}t$, where t is the duration of loading. In accordance with the aforementioned assumption regarding zero-stress within the shielding zones, only non-shielded portions of the brittle-material structure are associated with the internal stress level σ . To derive a relationship between the external stress (pertains to the entire bulk and surface domains) and the internal stress (pertains only to the unshielded portions of these domains) a scalar damage parameter, D , was defined as a ratio of the union of all shielding-zone volumes/surfaces and the structure volume/surface. This yielded the following relation:

$$\Sigma = \sigma(t)(1 - D(\sigma)) = \dot{\sigma}t(1 - D(\dot{\sigma}, t)) \quad (8)$$

where D is taken to depend on $\dot{\sigma}$ and t , since the product of the two is equal to σ and affects the density of crack nucleating flaws via Eq. (2), while t alone affects the size of the shielding zones via Eq. (6).

According to Eq. (8), as the loading duration increases, the $\sigma(t)$ increases causing Σ to increase while the $(1 - D(\sigma))$ term decreases causing Σ to decrease. Thus, there is a critical loading duration at which Σ reaches a maximum value and this value, Σ_{max} , is defined as the material dynamic strength. The material dynamic strength is then defined as:

$$\frac{d\Sigma}{d\sigma} = 0 \quad (9)$$

Before Eq. (9) could be utilized, an expression is required for the internal-stress dependence of the damage parameter. Towards that end and following Denoual and Hild [20,22], the damage parameter D is set equal to the probability of flaw shielding (i.e. the probability of finding a flaw within a shielding zone), P_{sh} , which is given in accordance with Eq. (1) as:

$$D = P_{sh} = 1 - \exp(-\lambda_t Z_{sh}) \quad (10)$$

where Z_{sh} is the average size of the shielding zone defined as:

$$\lambda_t(t)Z_{sh}(t) = \int_0^t \frac{d\lambda_t}{dt} \Big|_\tau [kC(t-\tau)]^n d\tau \quad (11)$$

When deriving Eq. (11), it was taken into account that the shielding zone average size Z_{sh} at time t , when the total flaw density is $\lambda_t(t)$, the crack in question could have been nucleated at any time, τ with $0 \leq \tau \leq t$ and that the corresponding shielding-zone size is $[kC(t-\tau)]^n$. In general, the probability for crack nucleation is not constant in the $[0, t]$ time interval but rather scales with the rate of activation of the flaws at time τ , given as $\frac{1}{\lambda_t(t)} \frac{d\lambda_t}{dt} \Big|_\tau$ with $\int_0^t \lambda_t(t) \frac{d\lambda_t}{dt} \Big|_\tau d\tau = 1$ (since for a shielding zone to exist the crack must have nucleated at some time in the $[0, t]$ time interval).

In the case of uniform loading under constant stress rate conditions considered here, and via Eq. (2), the term $\frac{d\lambda_t}{dt} \Big|_\tau$ can be written as:

$$\frac{d\lambda_t}{dt} \Big|_\tau = \frac{\lambda_0 m \dot{\sigma}^m t^{m-1}}{S_0^m} \quad (12)$$

After substitution of Eq. (12) into Eq. (11) and, in turn, into Eq. (10), and subsequent integration, the following internal-stress dependent damage-parameter function is obtained:

$$D = 1 - \exp \left(- \frac{m! n! \left(\frac{\sigma}{\sigma_c} \right)^{m+n}}{(m+n)!} \right) \quad (13)$$

where the characteristic internal stress σ_c is defined as:

$$\sigma_c = \dot{\sigma} t_c = \left[\frac{S_0^m \dot{\sigma}^n}{\lambda_0 S (kC)^n} \right]^{\frac{1}{m+n}} \quad (14)$$

Substitution of Eq. (13) into Eq. (8) and differentiation of the resulting equation in accordance with Eq. (9) yields:

$$\sigma|_{\Sigma_{max}} = \left(\frac{S_0^m \dot{\sigma}^n}{\lambda_0 S (kC)^n} \right)^{\frac{1}{m+n}} \left(\frac{(m+n-1)!}{m! n!} \right)^{\frac{1}{m+n}} \quad (15)$$

and

$$\sigma_{f,dynamic} = \Sigma_{max} = \sigma_c \left[\frac{1}{e} \frac{(m+n-1)!}{m! n!} \right]^{\frac{1}{m+n}} \quad (16)$$

where $\sigma_{f,dynamic}$ is the material average fracture strength in the fine-fragmentation mode. Substitution of Eq. (15) into Eq. (13) yields the following expression for the extent of material damage at the onset of cracking under high-loading rates:

$$D|_{\Sigma_{max}} = 1 - \left(\frac{1}{e} \right)^{\frac{1}{m+n}} \quad (17)$$

Furthermore, setting $\sigma = \dot{\sigma} t$ in Eq. (15) gives the duration of loading at the onset of dynamic fracture as:

$$t|_{\Sigma_{max}} = \left(\frac{S_0^m}{\lambda_0 S (kC)^n \dot{\sigma}^m} \right)^{\frac{1}{m+n}} \left(\frac{(m+n-1)!}{m! n!} \right)^{\frac{1}{m+n}} \quad (18)$$

2.3.3. Comparison between quasi-static and dynamic failure initiation

To help understand the relationship between coarse-fragmentation and fine-fragmentation failure/fracture modes for soda-lime glass, fracture strength vs. constant stress-rate plot is constructed and displayed in Fig. 1a and b for the bulk and surface failure, respectively. To assist in interpretation of these figures, a second horizontal axis, Z_{eff}/Z_c , is introduced where Z_c is the Z equivalent of σ_c . In both Fig. 1a and b, two fracture strength curves are displayed: (a) one corresponding to the average stress-rate independent quasi-static fracture strength, Eq. (3); and (b) the average dynamic fracture strength (increases with an increase in the stress-

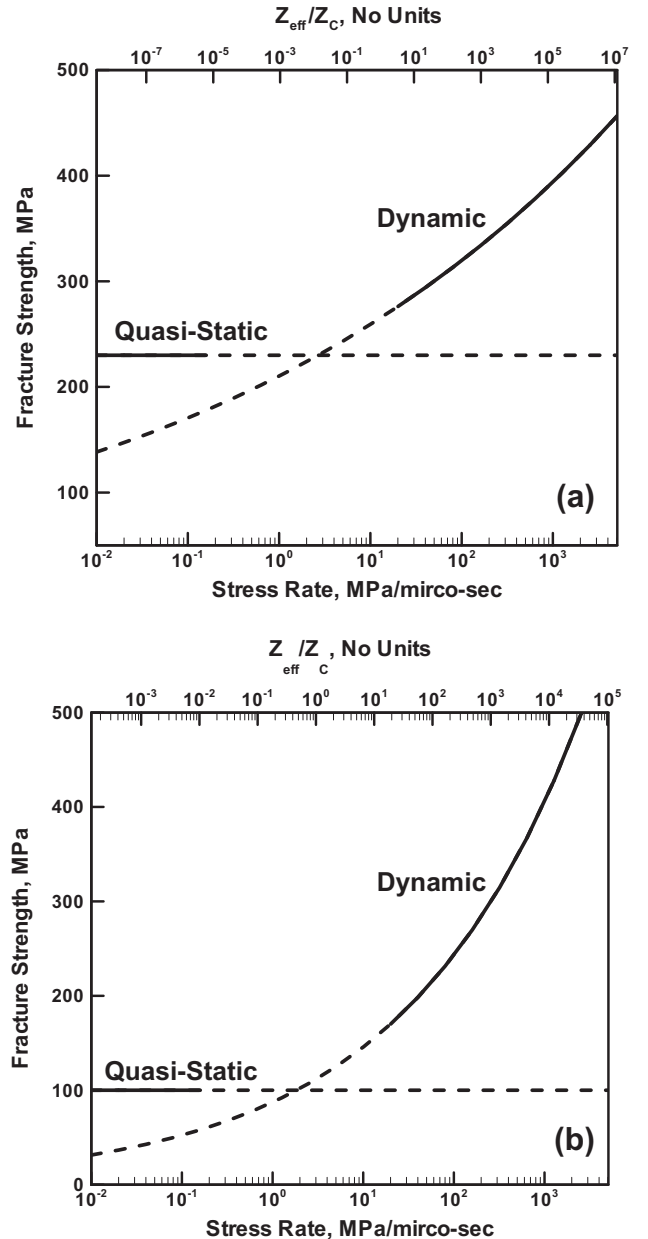


Fig. 1. The transition between the quasi-static (coarse fragmentation) and the dynamic (fine fragmentation) brittle-fracture modes as a function of an increase in stress rate for: (a) bulk; and (b) surface mode of fracture. See text or the explanation of Z_{eff} and Z_c .

rate), Eq. (16). The relevant quasi-static and dynamic fracture material-model parameters used in the construction of Fig. 1a and b are listed in Table 1.

It should be noted that in Fig. 1a and b, the two expressions for the (mean) fracture strength, Eqs. (3) and (16), are valid only over a limited range of stress rates and that the ranges are different for the two relations. That is, in the high stress rate range, defect shielding is less pronounced and, hence, the coarse-fragmentation fracture strength relation, Eq. (3), (which was based on an assumption of complete shielding of the surrounding material by the first nucleated crack) is not valid. On the other hand, the dynamic fracture strength relation, Eq. (16), is not valid in the low stress rate range (i.e. at lower values of Z_{eff}/Z_c), since in this case the size of the accompanying shielding zone at the onset of fracture exceeds the total domain size. The approximate stress-rate ranges of valid-

Table 1

Mechanical property parameters for soda-lime glass used in the present work.

Property	Symbol	Value	Unit
Young's modulus	E	70.0	GPa
Poisson's ratio	ν	0.22	N/A
Density	ρ	2500	kg/m ³
Mean fracture toughness	K_{IC}	0.75	MPa m ^{1/2}
<i>Weibull parameters for surface controlled fracture</i>			
Weibull modulus	m	7	N/A
Mean static fracture strength	$\sigma_{f,static}$	100	MPa
Effective surface	Z_{eff}	0.01	m ²
Weibull scale parameter ^a	$S_0/\lambda_0^{1/m}$	55.3	MPa m ^{2/m}
<i>Weibull parameters for volume controlled fracture</i>			
Weibull modulus	m	30	N/A
Mean static fracture strength	$\sigma_{f,static}$	230	MPa
Effective volume	Z_{eff}	10 ⁻⁴	m ³
Weibull scale parameter ^a	$S_0/\lambda_0^{1/m}$	186	MPa m ^{2/m}

^a Computed using Eq. (3).

ity for the two fracture-strength functions are indicated using “solid” lines in Fig. 1a and b. The intermediate stress-rate range is represented by the “dashed” portions of the curves. In general, within the intermediate stress-rate range, one would expect a monotonic transition between the low and high stress-rate branches. However, in the model of Grujicic et al. [4,5] the transition between the coarse-fragmentation mode and the fine-fragmentation mode was assumed to occur abruptly at a constant value of the stress rate (defined as the point of intersection of the two fracture-strength curves in Fig. 1a and b).

2.3.4. Damage-induced material property degradation

As discussed earlier, fine-fragmentation mode-induced damage causes degradation of the material stiffness and strength. In order to quantify the progression of material-property degradation, a damage evolution equation is required. Such an equation is obtained by differentiating Eq. (13) with respect to σ , to get:

$$dD/d\sigma = \frac{m!n!(m+n)\sigma^{m+n-1}}{(m+n)!\sigma_c^{m+n}}(1-D) \quad (19)$$

It should be noted that, within the soda-lime glass material model of Grujicic et al. [4,5], damage is assumed to be of an isotropic character so that the material remains isotropic during failure. Out of the two isotropic material elastic constants (Young's modulus and Poisson's ratio), only the Young's modulus is assumed to degrade.

Young's modulus of glass is then degraded according to the following relation:

$$E = E_0(1 - D) \quad (20)$$

where subscript 0 is used to denote a quantity pertaining to glass in its virgin state.

A comparison of Eqs. (8) and (20) shows that, in the multiple-fragmentation mode, the unshielded portions of the material are associated with the internal stress σ and the virgin-material Young's modulus, E_0 , while the entire unshielded + shielded material region is associated with the macroscopic stress, $\Sigma = \sigma(1 - D(\sigma))$ and the degraded Young's modulus, $E = E_0(1 - D)$.

2.4. Material-model parameterization

A summary of the soda-lime glass material-model parameters used in the present work is provided in Table 1. This summary contains the parameters assessed by Grujicic et al. [4,5] using the open-literature experimental and computational results and newly

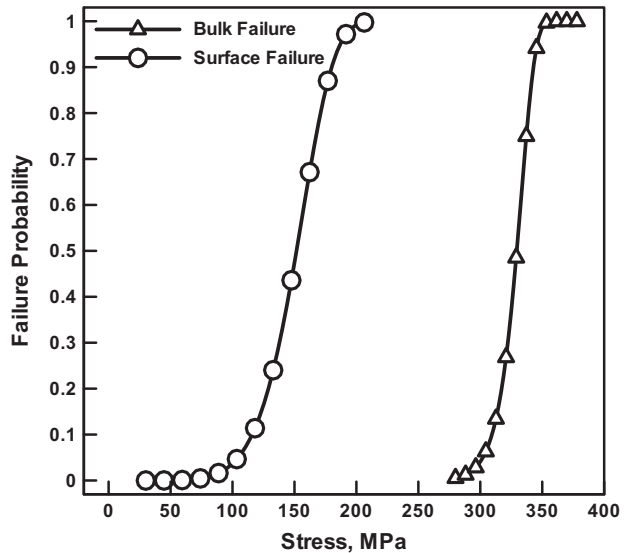


Fig. 2. Weibull-type failure probability curves for soda-lime glass in the case of bulk and surface modes of fracture.

assessed parameters. The new assessment involved the same open-literature data, but it was of a higher rigor.

The virgin-material elastic stiffness properties (including Young's modulus and Poisson's ratio), density, and the mode-I critical stress intensity factor listed are taken from Grujicic et al. [4,5]. The same is true for the bulk-controlled fracture parameters. The surface-controlled fracture parameters are obtained in the new assessment procedure. The failure probability functions for the bulk and the surface modes of failure based on the parameterization provided in Table 1 and a 1 cm³ (cube) soda-lime specimen are displayed in Fig. 2. As expected, surface fracture is associated with a lower level of the fracture strength and a broader distribution. As stated earlier, transition between the coarse-fragmentation and fine-fragmentation brittle-fracture modes is assumed to take place at a constant stress-rate. Based on the results displayed in Fig. 1a and b, this stress-rate was set to a value of 2.68 MPa/μs for the bulk fracture and 1.83 MPa/μs for the surface fracture.

In addition to the parameters listed in Table 1, the following conditions were defined: (a) in accordance with the previous discussion, the crack terminal velocity is set to a value equal to 30% of the material sound speed (the latter is calculated using the materials Young's modulus and density); and (b) as stated earlier, depending on the (bulk vs. surface) location of the flaws, the crack shielding zones are assumed to be either spherical or circular, respectively. Consequently, for the two cases, the dimensionality factor, n , and the shielding zone shape factor, S , are set to 3 and $4/3\pi$ for bulk failure, and 2 and π for surface failure.

As far as the linear-elastic fracture-mechanics based macro-crack growth model is concerned, it is associated with a single material parameter, i.e. the mode-I critical stress intensity factor, K_{IC} . In accordance with the stress-based macro-cracking initiation criterion, the mode-I critical stress intensity factor was taken, in the prior work of Grujicic et al. [4,5], to be a stochastic quantity and given by a Weibull-distribution function with the same reference defect density, λ_0 , and Weibull modulus, m , (have different values in the bulk and surface regions) as in the fracture strength case. As far as the scaling parameter is concerned, it was computed using an equation analogous to Eq. (3) and assuming a constant mean value of the mode-I critical stress intensity factor of 0.75 MPa m^{1/2} [20] (for both the bulk and surface regions). In the present work, K_{IC} was not considered to be a stochastic quantity.

This is not considered to be a simplification, but rather a physically more correct treatment of this quantity. That is, in brittle solids such as glass, K_{IC} is related to the material surface energy and the latter quantity (in the absence of large microstructure/compositional heterogeneities) is generally considered to be deterministic.

3. Soda-lime glass non-linearity and inelasticity

As explained earlier, the main objective of the present work is to examine (computationally) the role of material non-linearity and inelastic deformation behavior on the dynamic response of soda-lime glass. In this section, a brief description is provided of the basic physics for the two phenomena, their mathematical formulation, and their implementation into the soda-lime material model of Grujicic et al. [4,5].

3.1. Underlying physics

In the original model of Grujicic et al. [4,5], the material volumetric response was assumed to be linear elastic, both in compression and tension. This assumption is not fully consistent with a number of experimental findings [14,15] which showed that under sufficiently high pressures (greater than ca. 3.5 GPa) the compressive loading response of soda-lime glass becomes visibly nonlinear (material nonlinearity) and irreversible (inelastic). This behavior of soda-lime glass is depicted in the axial stress vs. normalized specific volume plot, Fig. 3, obtained in a standard flyer plate experiment [28]. Under hydrostatic tension, however, material fails at a relatively low pressure (less than ca. 300 MPa) and, prior to the onset of failure, the material response is linear elastic.

A literature review carried out as part of the present work established that there is no general consensus regarding the nature of the material intrinsic phenomena and processes responsible for the aforementioned nonlinearity and inelasticity of soda-lime glass. The following main theories appear noteworthy: (a) shear induced micro-cracking [29]. The main supporting evidence for this phenomenon is the experimental observation of reduced spallation strength in (compressively) pre-shocked soda-lime glass; (b) irreversible compaction characterized by permanent density increase and non-significant changes in the material bond structure and molecular-level topology e.g. [30]. The main supporting evidence in this case comes from post-mortem characterization of the mate-

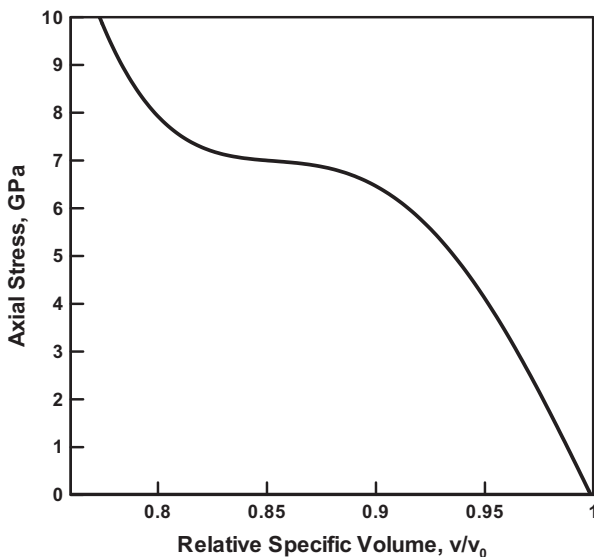


Fig. 3. Typical axial-stress vs. normalized specific volume response during dynamic-compressive loading and unloading.

rial density and microstructure; and (c) various phase transformations which are accompanied with both significant irreversible increases in material density and major changes in material bond structure and molecular-level topology [16]. As in the previous case, the main supporting evidence comes from post-mortem characterization of the material density and microstructure. In addition, molecular-level simulations of shock wave generation and propagation in soda-lime glass provided evidence for changes in the Si-atom coordination and Si-O ring topology in the as-shocked material state. An example of such molecular-level computational results obtained in our ongoing work is displayed in Fig. 4a and b.

3.2. Mathematical formulation

As discussed above, the origin of soda-lime glass non-linearity and inelasticity has not yet been fully established. This, however,

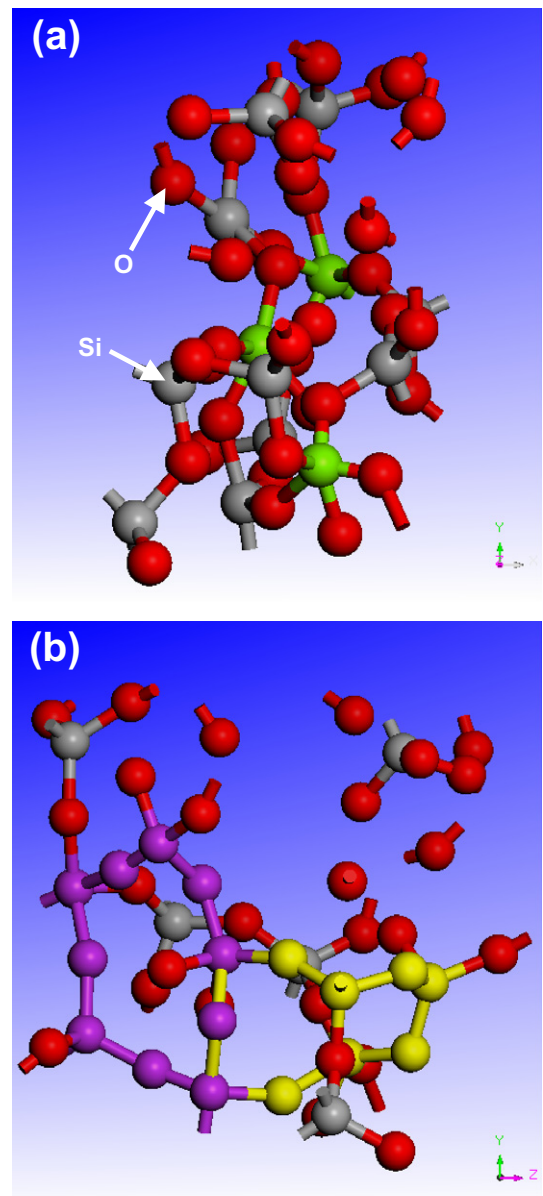


Fig. 4. Changes in the soda-lime glass bond structure and molecular-level topology under shock loading: (a) development of fivefold coordinated silicon atoms (highlighted in green); and (b) formation of smaller Si-O rings (highlighted in purple and yellow). (For interpretation of the references to color in this figure legend, the reader is referred to the web version of this article.)

is not a hindrance from the point of implementation of these phenomena as an enhancement to the continuum-level material model for soda-lime glass developed by Grujicic et al. [4,5]. In other words, by examining the experimental data published in the open literature, it was possible, within the present work, to quantify the extent of material nonlinearity and deformation irreversibility as a function of the maximum compressive pressure. It should be noted that the shear component of the material response is assumed to remain linear. In the remainder of this section, brief explanations are provided of the mathematical formulations used to quantify soda-lime glass nonlinearity and inelasticity.

The experimental data published in the open literature [28] are used to determine the dependence of soda-lime glass pressure on the normalized specific volume in the form:

$$P(v/v_0) = \begin{cases} k_1 + k_2(v/v_0) + k_3(v/v_0)^2, & \text{for } v/v_0 > 0.916 \\ k_4, & \text{for } 0.813 < v/v_0 < 0.916 \\ k_5 + k_6(v/v_0) + k_7(v/v_0)^2, & \text{for } v/v_0 < 0.813 \end{cases} \quad (21)$$

where $k_1 = -301.3$ GPa, $k_2 = 668.9$ GPa, $k_3 = -367.6$ GPa, $k_4 = 2.97$ GPa, $k_5 = 780$ GPa, $k_6 = -1920$ GPa and $k_7 = 1184$ GPa. Examination of Eq. (21) reveals the presence of three distinct v/v_0 (compressive) regions: (a) $0.916 < v/v_0 < 1.0$, the initial anomalous compression regime characterized by a continuous volumetric softening; (b) $0.813 < v/v_0 < 0.916$, the irreversible compaction regime; and (c) $v/v_0 < 0.813$, the normal compression regime characterized by continuous volumetric stiffening. Coefficients k_1 to k_7 are obtained by applying the conventional least-squares curve-fitting procedure to the experimental data reported in Ref. [28].

Eq. (21) is used in the present work in two different ways: (a) to define volumetric loading and unloading paths under the assumption that the material is non-linear. In this case, the tangent bulk modulus is defined using the negative slope of the P vs. v/v_0 curve; and (b) to define the loading path under the assumption that the material is linear-elastic and volumetrically-plastic. In other words, the P vs. v/v_0 curve represents the irreversible volumetric-strain hardening behavior of soda-lime glass. Unloading and elastic reloading, on the other hand, are taken to be associated with a linear-elastic material response and a volumetric-strain independent bulk modulus (equal to the bulk modulus of the virgin material, Table 1).

3.3. Implementation into a user-material subroutine

Mathematical formulation for the material nonlinearity and deformation inelasticity are used to enhance the continuum-level material model for soda-lime glass [4,5]. The resulting enhanced material model was coded using the Intel Fortran computational language and implemented as a *VUMAT Material User Subroutine* within the commercial finite element program ABAQUS/Explicit [31]. At the beginning of each analysis, the material subroutine is compiled and linked with the finite element solver which enables ABAQUS/Explicit to pass the necessary material state and deformation variables to the material model for each element integration point at each time step and subsequently receive back the updated material state and stress variables.

The basic procedure for coupling the ABAQUS/Explicit finite-element solver with the VUMAT Material User Subroutine at each time increment at each integration point of each element can be outlined as follows:

- (a) The finite-element integration-point-specific previous time-increment stresses and material state variables as well as the current time-step incremental strains are passed to the VUMAT by the ABAQUS/Explicit finite-element solver. Specifically, the glass material model formulation used in the

present work requires the following state variables to be passed into the VUMAT in addition to the requisite strain increment components: (i) material initial strength value, assigned randomly from the material-specific Weibull distribution (although this quantity does not change, it is treated as a state variable for practical/operational reasons); (ii) the extent of coherent damage; (iii) minimum specific volume achieved (to track irreversible densification); and (iv) a variable defining the deletion status of the element; and

- (b) Using the material state information passed to the VUMAT in (a), and the soda-lime glass material model presented in Section 2, the material stress state as well as the updated values of the material state variables are calculated and returned to the ABAQUS/Explicit finite-element solver. Additional information that is required to be updated, but not passed back to the solver, in order to handle the macro-cracking component of the material modeling includes the element location, failure status, and the direction of crack opening (where appropriate) which are stored in the form of globally available matrices.

4. Problem formulation and computational analysis

4.1. Problem formulation

To examine the effect of material non-linearity and inelasticity on the dynamic behavior of soda-lime glass, the case of a symmetric flyer plate impact is analyzed. Within this problem, a plate-like target is impacted by a plate-like projectile at a zero obliquity angle (normal impact). The target and projectile are composed of the same (soda-lime glass) material. The projectile thickness (5 mm, in the present case) is selected to be less than the target thickness (10 mm, in the present case) to ensure that the so-called *candidate spallation plane* lies within the target. In the limit of a large ratio of the target/projectile lateral dimensions to the thickness, the problem can be treated as being one-dimensional in character.

A schematic of the typical time, t vs. (Lagrangian-type) spatial coordinate, X , plot for the problem at hand is depicted in Fig. 5. Examination of this figure reveals the following: (a) at the moment of impact two centered simple waves are generated at the impact surface and propagate toward the projectile and target free surfaces. The reason that the impact does not generate shock waves is that soda-lime glass shows an anomalous concave downward P vs. v/v_0 behavior (at least within a 0–3 GPa range, analyzed in the present work), Fig. 3; (b) upon the reflection of these waves from the target/projectile free surfaces, two simple waves (with converging characteristics) are formed; and (c) two approaching simple waves intersect within a region marked by vertices a , b , c , and d , Fig. 5. The b , c , and d bounded portion of this region contains the material which first experiences tensile stresses. The candidate spallation plane is defined as the X -location within this region at which the tensile stress first becomes equal to the material fracture strength. Typically, spallation fracture initiates on this plane.

4.2. Computational analysis

4.2.1. Computational/geometrical domain(s)

As explained above, the problem at hand is of a one-dimensional character. The computational domain employed is composed of two Lagrangian regions, one representing the projectile and the other representing the target, Fig. 6. The dimension of the two regions in the impact direction is set equal to the respective plate thicknesses (defined above). The lateral dimensions are inconsequential to the computational results and thus are assigned arbitrarily large values to facilitate post-processing visualization.

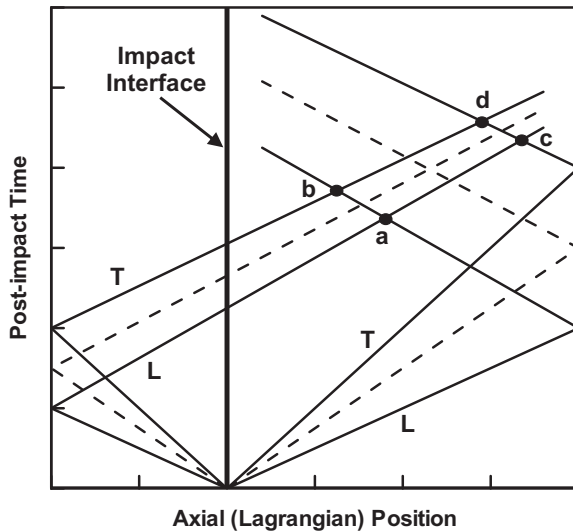


Fig. 5. Schematic of a typical time vs. (Lagrangian) spatial coordinate plot for a symmetric soda-lime glass flyer-plate impact. Note, T and L are used to denote the leading and trailing portions of the wave, respectively.

4.2.2. Finite element mesh

The two regions are meshed to each form a column of single elements running in the direction of impact. To determine the axial mesh dimension, the mesh was gradually refined until further refinement did not considerably affect the results. This procedure yielded the meshed axial dimension of 10 μm .

4.2.3. Material model

Due to the symmetric nature of the flyer-plate impact problem, the projectile and the target are composed of identical (soda-lime glass) material. This material is modeled represented using three different models: (a) the original model of Grujicic et al. [4,5]; (b) the present rendition of the this model which includes only additional nonlinear elastic effects; and (c) the present rendition of the this model which includes both additional nonlinear elastic and inelastic effects.

4.2.4. Initial conditions

At zero simulation time, the projectile is assigned an incident velocity in a 100–900 m/s range, while the target is assumed to be stationary.

4.2.5. Boundary conditions

Zero lateral velocity boundary conditions are applied to all the nodes in the model. This boundary condition ensures the uniaxial strain material state that is expected under flyer-plate impact conditions.

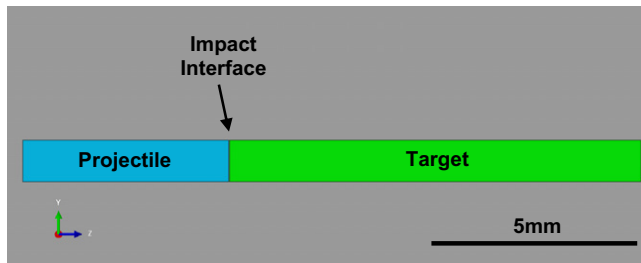


Fig. 6. The computational Lagrangian domain representing the projectile and the target plates.

4.2.6. Contact conditions

The projectile/target interaction is modeled using a “penalty” contact method within which the penetration of the surfaces into each other is resisted by linear spring forces/contact-pressure with values proportional to the depth of penetration. Within this algorithm, pressure is transmitted only when the two bodies are in contact and there is no limit to the magnitude of this contact pressure.

4.2.7. Computational method

The flyer-plate impact problem described above is analyzed computationally in the present work using a transient, non-linear dynamics, explicit, Lagrangian, finite element analysis. Further details regarding this method can be in our prior work [26]. It should be noted that no variable mass scaling algorithm was used to improve the computational efficiency due to the relatively low computational cost. Furthermore, due to the very fine nature of the mesh and the absence of shock waves, no bulk viscosity algorithm (aimed at mitigating the computational challenges associated with large field gradients) was used.

5. Results and discussion

In this section, the main results obtained in the aforementioned transient nonlinear dynamics computational analysis of the symmetric flyer-plate impact scenario are presented and discussed. Specifically, the results pertaining to the: (a) wave structure/motion/interaction; (b) target back-face velocity history analysis; and (c) impact velocity spallation threshold analysis.

5.1. Wave structure/motion/interaction

A typical particle-velocity field plot (at 8 equally-spaced, by 120 ns, post-impact times) for the case of the projectile/target material represented using the original soda-lime glass material model of Grujicic et al. [4,5] is displayed in Fig. 7. Within the impact scenario depicted in Fig. 7 (as well as in Figs. 8 and 9), the projectile was assigned an incident particle velocity of 200 m/s. Examination of Fig. 7 reveals: (a) the formation of two diverging compression waves emanating from the impact interface. The two waves bound a projectile/target region characterized by a particle velocity of ca. 100 m/s; (b) upon reflection of these waves from their respective free surfaces, two approaching release waves are formed. The right propagating release wave leaves an effectively stationary material in its wake, while the material behind the left propagating release wave acquires the particle velocity matching the projectile initial velocity; (c) upon the intersection of these two release waves, a tensile region bounded by the two (now diverging) release waves is formed. The existence of tensile stresses in this region is related to the fact that the material particles at the left boundary of this region are stationary while those at the right boundary move (to the right) at the projectile initial velocity; and (d) spall fracture takes place in this region along the candidate spall plane(s) resulting in the formation of a principal fragment (with a linear momentum nearly equal to that of the projectile prior to impact) of target material and several smaller fragments. Small fragments are formed as a result stress “ringing” following the formation of the principal fragment. While this artifact could be prevented by employing an artificial viscosity algorithm, this was not done in the present work in order to preserve the natural wave profiles. While the observations made are generally consistent with t vs. X plot shown in Fig. 5, there are a few points of disagreement. As will be more clearly shown in Fig. 9, these disagreements are mainly related to wave structure (wave front profile). Specifically, spreading of the compression waves

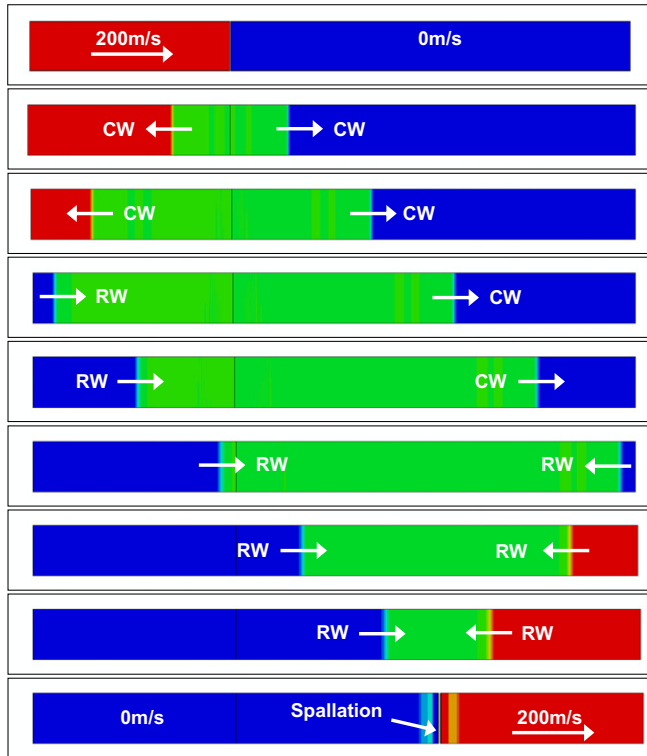


Fig. 7. A time-series (120 ns intervals) of particle-velocity field plots for the case of the projectile/target material represented using the original soda-lime glass material model of Grujicic et al. [4,5] and an initial flyer-plate velocity of 200 m/s.

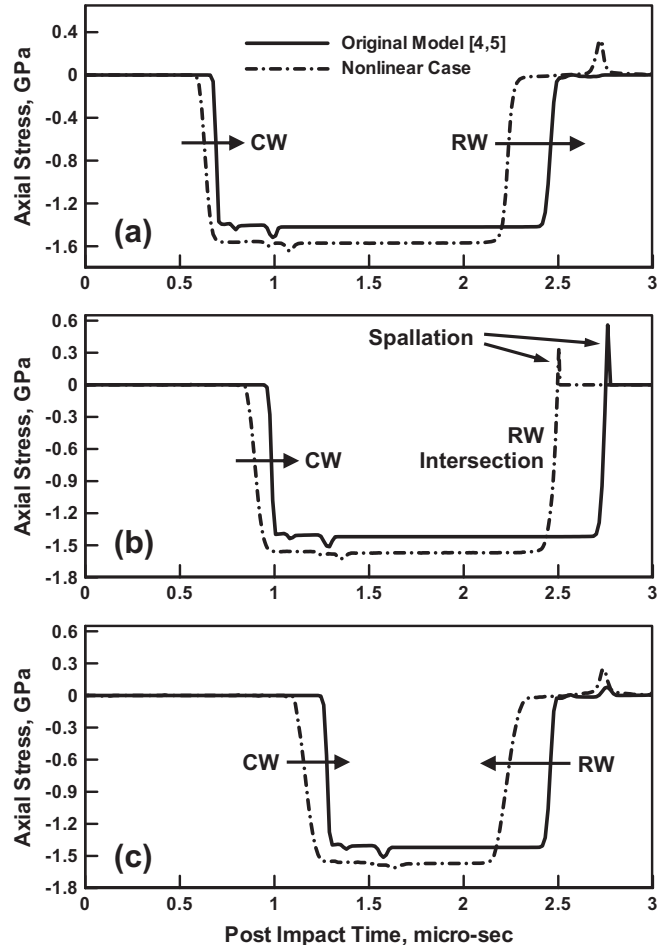


Fig. 9. Temporal evolution of the axial-stress at three different locations within the target: (a) a point close to the flyer-plate/target impact interface; (b) a point on the spall plane; and (c) a point close to the target back-face.

attendant linear elastic framework, both of these wave types are steady, weak elastic waves.).

The particle velocity field plot analogous to that displayed in Fig. 7, but for the case of the glass material model with the aforementioned nonlinear elastic modification, is shown in Fig. 8. The same four general observations regarding the wave propagation/reflection/interaction made are mirrored in Fig. 8. On the other hand, noticeable differences exist between the two sets of results regarding the wave structure/profile. Specifically, the results displayed in Fig. 8 provide clear evidence of compression wave spreading and release wave steepening. As mentioned earlier, these effects will be shown more clearly in Fig. 9.

The corresponding particle-velocity field plots for the case of the glass material model with the aforementioned nonlinear elastic and inelastic modifications are not shown since they are quite similar to the ones displayed in Fig. 8.

Temporal evolution of the axial-stress at three different locations within the target is displayed in Fig. 9a–c. The results displayed in Fig. 9a pertain to an element located near the projectile/target interface, those in Fig. 9b to an element within the spall region, while those in Fig. 9c pertain to an element near the target back-face. In each case, two curves are displayed corresponding to the material models employed in Figs. 7 and 8. Comparison of the results displayed in Fig. 9a–c clearly reveals spreading of the right propagating compression wave for the case of the nonlinear elastic material model. Furthermore, examination of Fig. 9a shows that the right

Fig. 8. A time-series (120 ns intervals) of particle-velocity field plots for the case of the projectile/target material represented using the nonlinear elastic material model and an initial flyer-plate velocity of 200 m/s.

and steepening of the release waves (expected in anomalous material like soda-lime glass) is not observed (since within the

propagating release wave has steepened considerably for the same material model case. No similar changes in the wave profile are apparent for the original soda-lime glass material model [4,5]. In passing, it should be noticed that upon the intersection of the two release waves, Fig. 9b, the stress first becomes tensile, upon spallation, retreats to zero stress.

5.2. Target back-face velocity history

The most common way of determining experimentally the shock hughoniot relations for a material is to employ flyer-plate experiments and measure the shock speed and the (upstream) particle velocity at different flyer-plate impact velocities. In these experimental procedures, free surface particle velocities are typically measured at the target back-face using various laser interferometry techniques. Subsequently, a computational procedure is employed to extract upstream particle velocities from the measured free-surface velocities. In this section, the results pertaining to the history of target back-face free-surface velocity are presented and discussed.

Temporal evolution of the target back-face particle velocities for the 200 m/s and 900 m/s projectile initial velocity cases is displayed in Fig. 10a and b, respectively. Three curves are shown in each figure corresponding to the three soda-lime glass material model cases.

Examination of the results displayed in Fig. 10a and b show that: (a) arrival of the right-propagating release wave, formed at the spallation-created free surface, to the target (now the principal fragment) back-face produces the so-called “pullback signal” (arrest and subsequent recovery of the back-face particle velocity); (b) in the lower flyer-plate impact velocity case, Fig. 10a, notable differences are observed in the free surface velocity history relative to the magnitude of the pullback signal. However, no similar differences are observed in the ultimate particle velocity achieved at the target back-face. In the context of the ballistic threat imposed by the principal “flying” spall fragment, the magnitude of the pull-back is less relevant than the ultimate particle velocity attained. It should be noted that only two curves in Fig. 10a are apparent due to identical low impact speed material response for the nonlinear-elastic and nonlinear-elastic/inelastic material model cases; and (c) in the higher flyer-plate impact velocity case, Fig. 10b, it is observed that all three material model cases again display a pullback signal, however, these signals are quite comparable in magnitude. It should be also noted that formation of additional finer non-principal fragments produces trailing pullback signals, in the case of the original soda-lime glass material model [4,5]. As far as the back-face ultimate particle velocities are concerned, they are significantly higher in original material model case.

5.3. Impact velocity spallation threshold

Spallation is a prominent damage/fracture phenomenon which is undesirable since it negatively affects the protection performance of a glass-based transparent armor system (e.g. vehicle/structure interior fragment release, degradation/loss of optical transparency, and decreased multi-hit performance). Hence, it is important to quantify spallation resistance of soda-lime glass and identify its sensitivity to the inclusion of non-linear and inelastic effects.

By carrying out a series of flyer plate impact simulations at increasing impact velocities, the critical impact velocity beyond which spallation takes place has been determined for each of the three aforementioned material model cases. Through this analysis procedure, it was observed that the critical impact velocity is ca. 25 m/s for all three cases considered. This finding is not unexpected since: (a) due to a low value of the fracture strength for

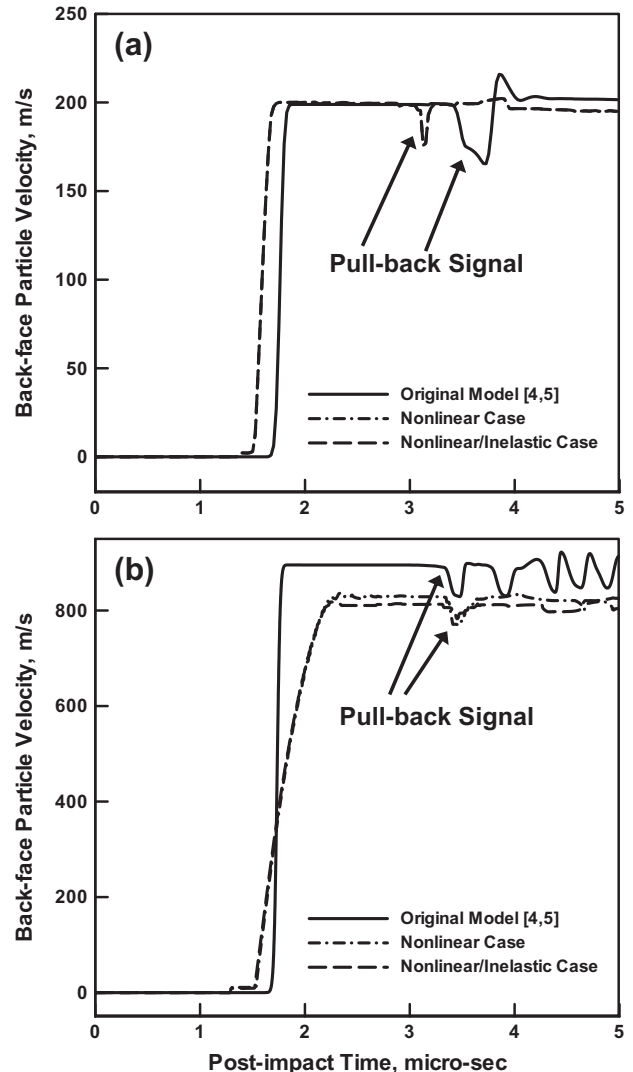


Fig. 10. Temporal evolution of the target back-face particle velocities for the case of flyer-plate impact velocities of: (a) 200 m/s; and (b) 900 m/s.

soda-lime glass, one should expect a relatively low value of the critical impact velocity; and (b) for the same reason, spallation occurs at a stress level where material nonlinearity and inelasticity effects make an insignificant contribution to the overall material response.

The finding presented above shows that protection performance of soda-lime glass as measured by the critical impact velocity is not dependent upon material nonlinearity and inelasticity. However, one may explore additional aspects of the impact performance of soda-lime glass. For example, momentum/kinetic energy carried by the propelled principal fragment is an important factor relative to the threat imposed by vehicle/structure-interior fragment release. In other words, lower values of the principal fragment linear momentum and kinetic energy are preferred in the case of spallation. To investigate this aspect of soda-lime glass impact performance, flyer-plate experiments are simulated at an impact velocity of 900 m/s. The results of these simulations for the three material model cases are displayed in Fig. 11a–c, respectively. Examination of the results displayed in these figures show that selection of material model affects both the size and the velocity of the principal fragment. Specifically, for the original, nonlinear elastic, and nonlinear elastic/inelastic soda-lime glass material models the linear momenta (scaled by the flyer-plate initial

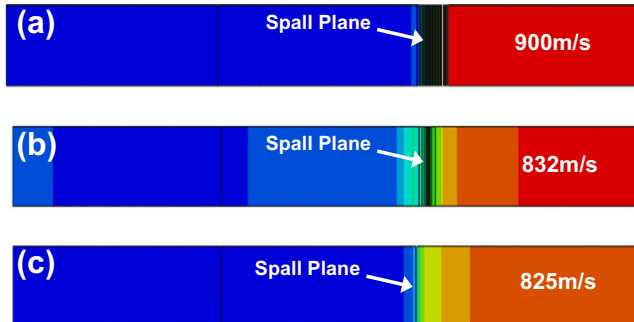


Fig. 11. Particle velocity field plots at a time shortly after spallation for the following material model cases for soda-lime glass: (a) the original formulation [4,5]; (b) the nonlinear elastic formulation; and (c) the nonlinear elastic/inelastic formulation.

momentum) are approximately 1.0, 0.88, and 0.90, respectively. The corresponding scaled kinetic energy of the principal fragment are approximately 1.0, 0.78, and 0.77, respectively. These findings suggest that nonlinear elasticity and inelastic deformation provide beneficial effects in reducing the linear momentum and kinetic energy of the principal fragment. It should be noted, that the observed reduction in the principal fragment linear momentum does not violate the principle of linear-momentum conservation since additional momentum remains in the flyer-plate/target. Also, at least a portion of the reduced kinetic energy of the principal fragment is associated with the permanent densification of a portion of the soda-lime glass material adjacent to the flyer-plate impact interface.

The findings reported above can be directly used during design of mass-efficient spallation-resistant transparent-armor systems. In our ongoing work, transparent armor design guidelines are being developed using the concept of material selection charts. The foundation for this approach is analogous to the one developed in our recent work [17].

It should be noted that experimental investigation of fracture phenomena (like spall fracture) under dynamic loading conditions in brittle materials is severely limited due to the accompanying massive destruction of the test samples. Furthermore, since spall fracture often controls ballistic performance of transparent armor systems, it is usually considered to be a sensitive subject matter. These are perhaps the two main reasons for paucity of relevant information in open literature. Typically, reported spall fracture studies involve the use of high-power lasers e.g. [32] to generate shocks (more precisely, short-duration shock pulses) rather than the use of ballistic impact tests e.g. [33]. Since a most comprehensive set of the open literature relevant experimental results identified in the present work are those reported in Ref. [32], an attempt is made in the remainder of this manuscript to correlate these experimental results with the present computational results. This was done while recognizing that the results in Ref. [32] were generated under shock pulse loading condition while the computational analysis carried out in the present work involved sustained shock loading. Comparison between the experimental and the computational results was done with respect to the effect of: (a) shock strength; and (b) target plate thickness on the size of the damage zone and the final size of the principal fragment.

Experimental results reported in Ref. [32] showed that an increase in the shock strength by 100% led to a 60–70% increase in the principal spall fragment size. The present computational results show that, the same increase in shock strength results in a ca. 70% increase in the principal spall fragment size. As far as the effect of target plate thickness is concerned, experiments in Ref. [32] show that an increase of this quantity by 200% resulted

in a decrease of the final size of the principal fragment by ca. 10%. The present computational results, on the other hand, show that the principal spall-fragment size is independent of the target thickness but rather scales directly with the flyer plate (projectile) thickness. It should be noted here that the effect of the target thickness observed in Ref. [32] is mainly associated with the extent of change in the shock pulse profile during its propagation through the target. On the other hand, sustained shocks used in the present computational work are not affected by the target-plate thickness. Based on the aforementioned outcome of the experiment/computation comparison, it can be concluded that the present model yields results which are generally consistent with the open literature-reported experimental results.

6. Conclusions

Based on the material-model development procedure utilized and the results of the subsequent computational analyses, the following main summary remarks and conclusions can be drawn:

1. The effect of material nonlinearity and inelastic behavior on the dynamic response (including spallation) of soda-lime glass is studied under symmetric flyer-plate loading conditions using computational methods and tools.
2. The nonlinear elastic and inelastic effects are incorporated into the high strain-rate, high-pressure, large-strain material model for soda-lime ballistic glass recently proposed by the authors.
3. The flyer-plate impact simulation results revealed that inclusion of nonlinear elastic and inelastic effects do not measurably affect spall resistance (as measured by a minimum flyer-plate velocity resulting in spallation).
4. However, these phenomena are found to yield beneficial effects associated with linear-momentum/kinetic energy reduction effects in the spall fragments.

Acknowledgments

The material presented in this paper is based on work supported by the US Army/Clemson University Cooperative Agreements W911NF-04-2-0024 and W911NF-06-2-0042 and by the Army Research Office (ARO) research contract entitled “Multi-length Scale Material Model Development for Armor-grade Composites”, Contract Number W911NF-09-1-0513.

References

- [1] Strassburger E, Patel P, McCauley JW, Kovalchick C, Ramesh KT, Templeton DW. High-speed transmission shadowgraphic and dynamic photoelasticity study of stress wave and impact damage propagation in transparent materials and laminates using the edge-on impact method. In: Proceedings of the 23rd international symposium on ballistics, Spain; April; 2007.
- [2] Strassburger E, Patel P, McCauley W, Templeton DW. Visualization of wave propagation and impact damage in a polycrystalline transparent ceramic – AION. In: Proceedings of the 22nd international symposium on ballistics, Vancouver, Canada; November 2005.
- [3] AMPTAC quarterly: army materials research: transforming land combat through new technologies, vol. 8, no. 4; 2004.
- [4] Grujicic M, Pandurangan B, Coutris N, Cheeseman BA, Fountzoulas C, Patel P, et al. A simple ballistic material model for soda-lime glass. Int J Impact Eng Int J Impact Eng 2009;36:386–401.
- [5] Grujicic M, Pandurangan B, Bell WC, Coutris N, Cheeseman BA, Fountzoulas C, et al. An improved mechanical material model for ballistic soda-lime glass. J Mater Eng Perform 2010;18(8):1012–28.
- [6] Sun DZ, Andreux F, Ockewitz A. Modeling of the failure behavior of windscreens and component tests. In: 4th LS-DYNA users’ conference, Bamberg, Germany; 2005.
- [7] Zarzycki T. Glasses and the vitreous state. Cambridge, UK: Cambridge University; 1991.
- [8] Nghiem B. Fracture du verre et hétérogénéité à l'échelle submicronique. PhD thesis, University of Paris 6, France; 1998 [in French].

[9] Brajer X, Forquin P, Gy R, Hild F. The role of surface and volume defects in the fracture of glass under quasi-static and dynamic loadings. *J Non-Cryst Solids* 2003;316:42–53.

[10] Guillemet C. In: Kurkjian CR, editor. Strength of inorganic glass. New York: Plenum; 1985.

[11] Kshinka BA, Perrela S, Nguyen H, Bradt RC. Strengths of glass spheres in compression. *J Am Ceram Soc* 1986;69(6):467–72.

[12] Gy R, Guillemet C. In: Pye LD, La Course WC, Stevens HJ, editors. The physics of non-crystalline solids. London: Taylor and Francis; 1992.

[13] Woodcock LV, Angell CA, Cheeseman P. Molecular dynamics studies of the vitreous state: simple ionic systems and silica. *J Chem Phys* 1976;65:1565–77.

[14] Valle RGD, Venuti E. High-pressure densification of silica glass: a molecular-dynamics simulation. *Phys Rev B* 1996;54(6):3809–16.

[15] Trachenko K, Dove MT. Densification of silica glass under pressure. *J Phys Condens Matter* 2002;14:7449–59.

[16] Liang Y, Miranda CR, Scandolo S. Mechanical strength and coordinate defects in compressed silica glass: molecular dynamics simulations. *Phys Rev B* 2007;75:024205.

[17] Grujicic M, Xie X, Arakere G, Grujicic A, Wagner DW, Vallejo A. Multidisciplinary optimization for fiber-glass reinforced epoxy-matrix composite 5MW horizontal-axis wind-turbine blades. *J Mater Eng Perform* 2010;19(8):1116–27.

[18] Grujicic M, Pandurangan B, King AE, Runt J, Tarter J, Dillon G. Multi-length scale modeling and analysis of microstructure evolution and mechanical properties in polyurea. *J Mater Sci* 2011;46(6):1767–79.

[19] Grujicic M, Pandurangan B, Bell WC, Cheeseman BA, Yen C-F, Randoow CL. Molecular-level simulations of shock generation and propagation in polyurea. *Mater Sci Eng A* 2011;528(10–11):3799–808.

[20] Denoual C, Hild F. Dynamic fragmentation of brittle solids: a multi-scale model. *Eur J Mech Solids A* 2002;21:105–20.

[21] Yazdchi M, Valliappan S, Zhang W. A continuum model for dynamic damage evolution of anisotropic brittle materials. *Int J Numer Methods Eng* 1996;39:1555–83.

[22] Hild F, Denoual C, Forquin P, Brajer X. On the probabilistic and deterministic transition involved in a fragmentation process of brittle materials. *Comput Struct* 2003;81:1241–53.

[23] Grujicic M, Pandurangan B, Coutris N, Cheeseman BA, Fountzoulas C, Patel P, et al. A ballistic material model for Starphire®, a soda-lime transparent armor glass. *Mater Sci Eng A* 2008;492(1):397–411.

[24] Holmquist TJ, Templeton DW, Bishnoi KD. Constitutive modeling of aluminum nitride for large strain high-strain rate, and high-pressure applications. *Int J Impact Eng* 2001;25:211–31.

[25] Camacho GT, Ortiz M. Computational modeling of impact damage in brittle materials. *Int J Solids Struct* 1996;33(20–22):2899–938.

[26] Grujicic M, Bell WC, Pandurangan B, He T. Blast-wave impact-mitigation capability of polyurea when used as helmet suspension pad material. *Mater Des* 2010;31:4050–65.

[27] Bless S, Chen T. Impact damage in layered glass. *Int J Fract* 2010;162(1–2):151–8.

[28] Alexander CS, Chhabildas LC, Reinhart WD, Templeton DW. Changes to the shock response of fused quartz due to glass modification. *Int J Impact Eng* 2008;35:1376–85.

[29] Grady DE. Shock-wave compression of brittle solids. *Mech Mater* 1998;29:181–203.

[30] Cagnoux J. Analysis d'Échantillons d'Al₂O₃, TiB₂ et SiC Recuperes Apres des Chocs Allamt Jusqu'a 20 GPa. In: DYMAT 94 international conference on mechanical and physical behaviour of materials under dynamic loading, les Editions de Physique; 1994. p. 257–62.

[31] ABAQUS version 6.10, user documentation. Dassault Systems; 2011.

[32] de Ressegueir T, Cottet F. Spallation of glass materials under laser-induced shocks. *J Phys IV* 1994;4:C8629–34.

[33] Nyongue A, Azari Z, Abbadi M, Dominik S, Hanim S. Glass damage by impact spallation. *Mater Sci Eng A* 2005;407:256–64.